

# The Role of Calcium in Regulating the Conformational Dynamics of D-Galactose/D-Glucose-Binding Protein Revealed by Markov State Model Analysis

Maohua Yang,<sup>#</sup> Yegen Tang,<sup>#</sup> Jingwei Weng,<sup>\*</sup> Zhijun Liu,<sup>\*</sup> and Wenning Wang<sup>\*</sup>

 Cite This: *J. Chem. Inf. Model.* 2021, 61, 891–900

 Read Online

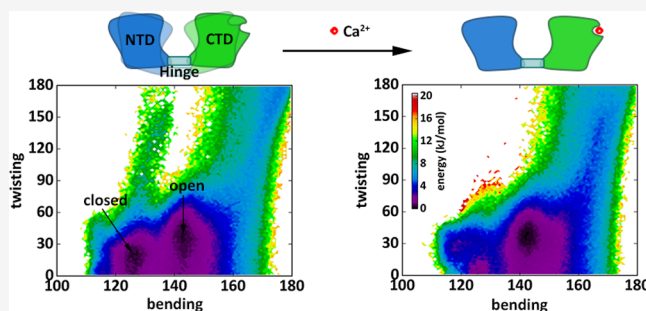
ACCESS |

 Metrics & More

 Article Recommendations

 Supporting Information

**ABSTRACT:** The D-glucose/D-galactose-binding protein (GGBP) from *Escherichia coli* is a substrate-binding protein (SBP) associated with sugar transport and chemotaxis. It is also a calcium-binding protein, which makes it unique in the SBP family. However, the functional importance of  $\text{Ca}^{2+}$  binding is not fully understood. Here, the calcium-dependent properties of GGBP were explored by all-atom molecular dynamics simulations and Markov state model (MSM) analysis as well as single-molecule Förster resonance energy transfer (smFRET) measurements. In agreement with previous experimental studies, we observed the structure stabilization effect of  $\text{Ca}^{2+}$  binding on the C-terminal domain of GGBP, especially the  $\text{Ca}^{2+}$ -binding site. Interestingly, the MSMs of calcium-depleted GGBP and calcium-bound GGBP (GGBP/ $\text{Ca}^{2+}$ ) demonstrate that  $\text{Ca}^{2+}$  greatly stabilizes the open conformation, and smFRET measurements confirmed this result. Further analysis reveals that  $\text{Ca}^{2+}$  binding disturbs the local hydrogen bonding interactions and the conformational dynamics of the hinge region, thereby weakening the long-range interdomain correlations to favor the open conformation. These results suggest an active regulatory role of  $\text{Ca}^{2+}$  binding in GGBP, which finely tunes the conformational distribution. The work sheds new light on the study of calcium-binding proteins in prokaryotes.



## INTRODUCTION

Substrate-binding proteins (SBPs), a large protein superfamily, are associated with membrane protein complexes for transport or signal transduction.<sup>1–8</sup> Despite their sequence diversity, their overall three-dimensional structure fold is highly conserved.<sup>9</sup> All SBPs consist of two globular Rossmann fold domains, connected by a hinge region.<sup>10,11</sup> D-glucose/D-galactose-binding protein (GGBP) belongs to a subclass of SBPs.<sup>9,12</sup> It participates in D-glucose/D-galactose transport associated with the MglABC transporter and facilitates chemotaxis.<sup>13,14</sup> Like most SBPs, GGBP has two globular domains, and its hinge region consists of three peptide segments.<sup>15,16</sup> The structures of *Escherichia coli* GGBP have been solved in both open and closed conformations with or without ligand binding.<sup>15–20</sup> Previous studies proposed that GGBP conformational dynamics plays a key role during ligand binding following a conformational selection mechanism coupled to a final rearrangement which obeys an induced-fit model.<sup>21,22</sup> Because of its reversible binding ability to sugars, GGBP is also a promising candidate for glucose biosensors.<sup>23–25</sup>

The unique feature of GGBP among the SBP family is that it is a calcium-binding protein.  $\text{Ca}^{2+}$  ion is bound at the C-terminal domain of GGBP (Figure 1a), which contains a EF-hand like  $\text{Ca}^{2+}$ -binding site consisting of a nine-residue loop

and a distantly located glutamate residue (Glu205).<sup>16</sup> The role of  $\text{Ca}^{2+}$  in eukaryotes has been extensively explored, but in prokaryotes the role of  $\text{Ca}^{2+}$  still remains elusive.<sup>26</sup> The function of  $\text{Ca}^{2+}$  in GGBP has always been a concern since the finding of the calcium-binding feature.<sup>16,27–29</sup> Infrared and fluorescence studies found that calcium depletion remarkably reduces the thermal stability of GGBP, and the C-terminal domain is more affected.<sup>27,28</sup> Heat denaturation study showed that unfolding of  $\text{Ca}^{2+}$ -bound GGBP is reversible and only incubation of the unfolded protein at a high temperature leads to an irreversible process.<sup>29</sup> It was also found that  $\text{Ca}^{2+}$  could only stabilize the structure of GGBP in the absence of sugar ligands.<sup>29</sup> All these studies point out the structural role of  $\text{Ca}^{2+}$  in GGBP, but the atomic details of the  $\text{Ca}^{2+}$ -dependent properties of GGBP and the potential effect on protein conformational dynamics remains elusive.

Recently, molecular dynamics (MD) simulation<sup>30</sup> combined with Markov state model (MSM) analysis<sup>31–35</sup> has been

Received: September 24, 2020

Published: January 14, 2021



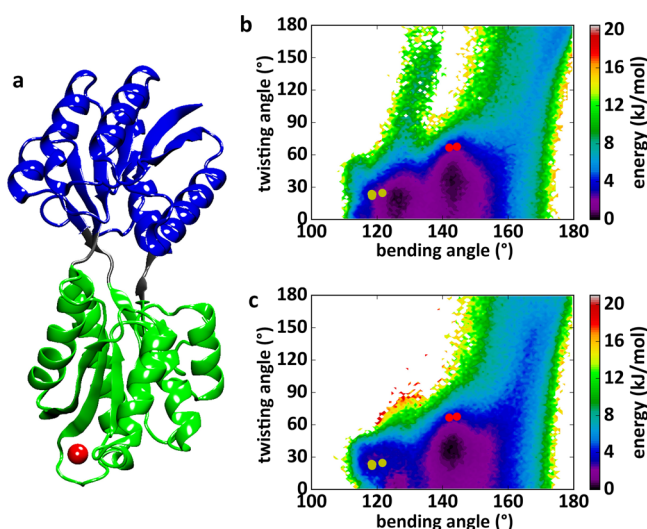


**Figure 1.** Free energy landscapes of apo-GGBP and GGBP/Ca<sup>2+</sup>. (a) Crystal structure of ligand-free *E. coli* GGBP/Ca<sup>2+</sup> (PDB ID: 2FW0). The N-terminal domain, C-terminal domain, and hinge region are colored in blue, green, and gray, respectively. Ca<sup>2+</sup> is shown by the red CPK model. (b) 2D-PMF of apo-GGBP. (c) 2D-PMF of GGBP/Ca<sup>2+</sup>. Yellow and red circles represent various crystal structures of the closed and open conformations of *E. coli* GGBP.

successfully applied in studies of protein folding,<sup>36–38</sup> molecular recognition<sup>39–44</sup> and conformational dynamics.<sup>45–48</sup> It reproduce the long-time conformational dynamics of biomolecules using data from short MD trajectories, yielding coarse-grained representations that are readily understandable.<sup>33,49</sup> Here, we performed unbiased all-atom MD simulations in explicit solvent and built MSMs to elucidate the role of Ca<sup>2+</sup> in the structural stability and conformational dynamics of GGBP from *E. coli*. Microsecond MD trajectories were accumulated for both Ca<sup>2+</sup>-free and Ca<sup>2+</sup>-bound GGBP (apo-GGBP and GGBP/Ca<sup>2+</sup>, respectively). It was found that Ca<sup>2+</sup> markedly stabilizes the open conformation of GGBP. The community network analysis reveals that Ca<sup>2+</sup> binding disturbs the hydrogen bonding interactions and weakens the connection between the C-terminal domain and the hinge region. The possible functional role of Ca<sup>2+</sup> is also discussed.

## MATERIALS AND METHODS

**MD Simulations.** The initial structures of MD simulations include the four closed (2FVY, 2GBP, 2HPH, and 1GLG) and the two open (2QW1 and 2FW0) crystal structures of *E. coli* GGBP.<sup>17–20</sup> For each crystal structure, we prepared two different simulation systems: apo-GGBP and GGBP/Ca<sup>2+</sup>. All systems were solvated with water molecules, and Na<sup>+</sup> and Cl<sup>−</sup> were added to obtain a salinity of 0.1 M and maintain neutral total charge (Table S1). There are in total ~73,850 atoms in each simulation box with a size of 1.015 nm × 1.015 nm × 1.015 nm. Periodic boundary conditions were applied in all three dimensions. All systems were energy-minimized by 5000 steps by using the steepest descent method. A 100 ps equilibration with the protein backbone restrained was performed before the production run.

All simulations were performed with Gromacs 5.0.<sup>50</sup> The force field Amber99SB<sup>51</sup> was used for protein and the TIP3P model<sup>52</sup> for water. Temperature was maintained at 300 K individually for the protein and for the solvent by the Berendsen weak coupling method with a time constant of

0.1 ps.<sup>53</sup> The pressure of the system was maintained at 1 bar by the same weak coupling method with a time constant of 5 ps.<sup>53</sup> All covalent bond lengths were constrained by LINCS,<sup>54</sup> allowing a time step of 2 fs. The van der Waals interaction cutoff was set at 1.2 nm. Electrostatic interactions were calculated by the particle mesh Ewald method with a cutoff of 1.2 nm.<sup>55</sup> The coordinates of the protein were saved every 100 ps.

In order to obtain sufficient sampling, we applied three rounds of simulations for both apo-GGBP and GGBP/Ca<sup>2+</sup> systems. For the first round of simulations, three 500 ns trajectories were conducted for each initial structure, and in total, 9 μs trajectories were generated for six initial structures (6 × 3 × 500 ns = 9 μs for six starting structures). All the MD conformations from the first-round simulations were collected for seeding subsequent unbiased MD simulations. In the second round of simulations, the conformations were divided into 100 groups using the k-center clustering algorithm based on the root-mean-square deviation (RMSD) value of all the 305 Cα atoms after aligning them. One center conformation was extracted from each cluster and used as the seed for one 200 ns MD simulation in the second round. Therefore, we in total collected 100 × 200 ns = 20 μs trajectories in the second round of simulations. In the similar way, the structures of the second round simulation were clustered into 100 clusters. One center conformation from each cluster was selected to initiate a new 200 ns trajectory as the third round of MD simulations. Finally, we obtained 218 trajectories summing up to ~49 μs for each system (apo-GGBP and GGBP/Ca<sup>2+</sup>, respectively).

**MSM Analysis.** MSM analysis is a powerful tool for turning swarms of short trajectories into a scientifically meaningful model of dynamics.<sup>31–33</sup> MSM analysis partitions phase space into a number of states, the transitions inside which are fast but transitions between which are slow. This separation of time scales ensures that the obtained model is Markovian and allows the construction of MSM from many short trajectories. The interconversion dynamics between the states can then be propagated to a longer time scale:

$$P(n\tau) = [T(\tau)]^n P(0)$$

in which  $T(\tau)$  is the transition probability matrix with a time interval  $\tau$ ,  $P(n\tau)$  is the vector of state population at time  $n\tau$ , and  $P(0)$  is the vector of initial state population. Here, all the MSMs were built using PyEMMA software 2.5.5.<sup>56,57</sup> All the trajectories were used for MSM construction. First, all the conformations for each system were clustered into 200 clusters by the k-center algorithm. The RMSD of Cα-atoms of all 305 residues was used for calculating the distance between two conformations. Then we counted the number of the transitions between each pair of microstates at a certain time interval (lag time) to construct the transition count matrix  $C$ . The element  $C_{ij}$  corresponds to the number of transitions from state  $i$  to state  $j$ . For the apo-GGBP system, we removed one cluster because it does not have connection with others. We then obtained the transition probability matrix through imposing detailed balance constraints on the transition count matrix and normalizing the matrix by row. To determine the lag time  $\Delta t$  when the system becomes Markovian, we examined the implied timescales ( $\tau_k$ ),<sup>31,32,58</sup> which is calculated as:

$$\tau_k = -\frac{\tau}{\ln \lambda_k(\tau)},$$

where  $\lambda_k(\tau)$  is the  $k$ th eigenvalue of the transition probability matrix  $T$  at a lag time  $\tau$ . The eigenvector whose associated eigenvalue is 1 is ignored in the calculation of implied timescale. This eigenvector reflects the stable equilibrium distribution of each state when the Markovian requirement is satisfied, and was used to calculate potential of mean force (PMF) along selected variables. The lag time was selected when the implied timescales are independent of lag time (Figure S1). In addition to the implied timescale test, our models were also validated by the Chapman–Kolmogorov test.<sup>59</sup> (Figure S2)

All the analyses for the apo-GGBP and GGBP/Ca<sup>2+</sup> were done on the basis of the MSM ensembles. Every ensemble contains 100,000 frames whose weights are derived from the equilibrium distribution of states.

**Calculation of the PMF.** The PMF  $W(s)$  along the reaction coordinate  $s$  is estimated through

$$W(s) = -k_B T \ln N(s) + C,$$

where  $T$  is the temperature,  $k_B$  is the Boltzmann constant,  $C$  is a constant selected to ensure the minimum of PMF is zero,<sup>35</sup> and  $N(s)$  is the accumulated weighted number of structures in the bin at  $s$ . One hundred conformations were randomly selected from each microstate for the calculation of  $N(s)$ , and each conformation is weighted by the population of state to which the structure belongs.

**Community Network Analysis.** Community network analysis is used to obtain an accurate picture of network topology and long-range signaling in protein complexes.<sup>60,61</sup> Here, we constructed the networks for apo-GGBP and GGBP/Ca<sup>2+</sup> based on MSM ensembles using the NetworkView plugin in visual MD.<sup>62,63</sup> Each residue was assigned to a node centered on its C $\alpha$  atom and used as a node to construct significant regions of amino acid interactions and pathways of allosteric modulation that connect them. Edges are added to the network by connecting pairs of “in-contact” nodes, which are defined as having any heavy atom within 4.5 Å for greater than 75% of the simulation time. Each edge is weighted by the correlation values ( $C_{ij}$ ) of the two end nodes as  $w_{ij} = -\log(|C_{ij}|)$ . The Girvan–Newman algorithm was used to divide the network map into communities of highly intraconnected but loosely interconnected nodes<sup>64</sup> in which the number of the shortest paths that cross a given edge (“betweenness”) is first calculated for all edges and the edge with the greatest betweenness is removed. This process is repeated and a modularity score is tracked to identify the division that results in an optimal community network. Critical nodes located at the interface of neighboring communities and the connecting edges that describe the probability of information transfer (betweenness) are then obtained.

**Protein Preparation.** The gene of *Escherichia coli* GGBP (without signal peptide) was cloned into the pET-28a+ vector with a His<sub>6</sub> tag at the N-terminal of the resulting protein. All of the mutations were created through a standard polymerase chain reaction-based mutagenesis method and confirmed by DNA sequencing. Recombinant proteins were expressed in *E. coli* BL21 (DE3) host cells at 16 °C and were purified by using Ni<sup>2+</sup>-NTA affinity chromatography followed by size-exclusion chromatography.

To remove the bound sugar ligands and Ca<sup>2+</sup> ions from GGBP, the purified protein was denatured with guanidine hydrochloride, and then dialyzed against refolding buffer (20 mM Tris pH 8.0, 100 mM NaCl). After concentration,

monomeric recombinant GGBP was isolated by size-exclusion chromatography. To prepare the protein samples for nuclear magnetic resonance (NMR) experiments, uniformly <sup>2</sup>H, <sup>15</sup>N-labeled GGBP proteins were prepared by growing bacteria in M9 minimal medium using <sup>15</sup>NH<sub>4</sub>Cl and <sup>2</sup>H<sub>2</sub>O as the sole nitrogen and carbon sources. All NMR samples were dissolved in 90% H<sub>2</sub>O, 10% D<sub>2</sub>O.

**Single-Molecule Förster Resonance Energy Transfer Experiments.** The double cysteine mutant GGBP proteins were labeled with the donor (Alexa Fluor 555-maleimide, Thermo Fisher Scientific Inc., MA, USA) and acceptor (Alexa Fluor 647-maleimide, Thermo Fisher Scientific Inc., MA, USA) by following the vendor provided protocol. The unreacted dye was separated from the labeled protein by using size-exclusion chromatography.

The glass coverslip and glass slide were cleaned by sonicating in water and ethanol three times, then etched in a plasma cleaner (PDC-002, Harrick Plasma Inc., NY, USA) for 5 min to destroy the residual dust further. Then the coverslip was stuck on the bottom of the drilled glass slide to make a flow cell. The flow cell was incubated with functionalized polyethylene glycol (PEG), with poly lysine and NTA (PLL(20)-g(3.5)-PEG(2)-NTA, SuSoS AG Inc., Switzerland) on each side to immobilize the labeled proteins. The single-molecule Förster resonance energy transfer (smFRET) images were taken by using a home-built wide-field fluorescence imaging system with an exposure time of 100 ms. The smFRET time trace was extracted from the image by using iSMS software.<sup>65</sup> The fluorescence intensity trace of single molecules was calculated using Matlab (Mathworks Inc., MA, USA) program to obtain the statistical histogram of FRET.

To estimate the smFRET efficiency, we calculated the  $C_\alpha$  distance of the three pairs of labeling sites for the frames from the MSM ensembles. The distances were converted into the smFRET efficiency according to Förster’s theory,<sup>66</sup>

$$E = \frac{1}{1 + \left(\frac{r}{R_0}\right)^6}$$

where  $r$  is the distance between the donor and the acceptor.  $R_0$  is the distance between the donor and the acceptor at which energy transfer is 50%. Here,  $R_0$  was set to 51 Å.<sup>67</sup>

## RESULTS

**Apo-GGBP Has High Conformational Flexibility.** First, we performed three rounds of MD simulations to explore the conformational space of apo-GGBP with an aggregated simulation time of 49.34  $\mu$ s. A MSM with 199-microstates was constructed with a lag time of 40 ns (Figure S1a, see Methods for more details). The model is also well validated by the Chapman–Kolmogorov convergence test (Figure S2a). The two-dimensional (2D) free energy landscapes (or PMF) as a function of the interdomain bending and twisting angles were calculated based on the MSM (Figure 1b). We also tried to use the tICA method to construct the MSM (Figure S3, see the Supporting Information for more details). The obtained 50-state MSM gives almost the same 2D-PMF (Figure S4). Although projections on selected coordinates in principle result in loss of information about other degrees of freedom, this procedure helps to capture features of dynamic processes in terms of interdomain motions. On this 2D-PMF, two energy minima (bending angle: 120° ~ 135°, twisting angle: 0° ~ 30°



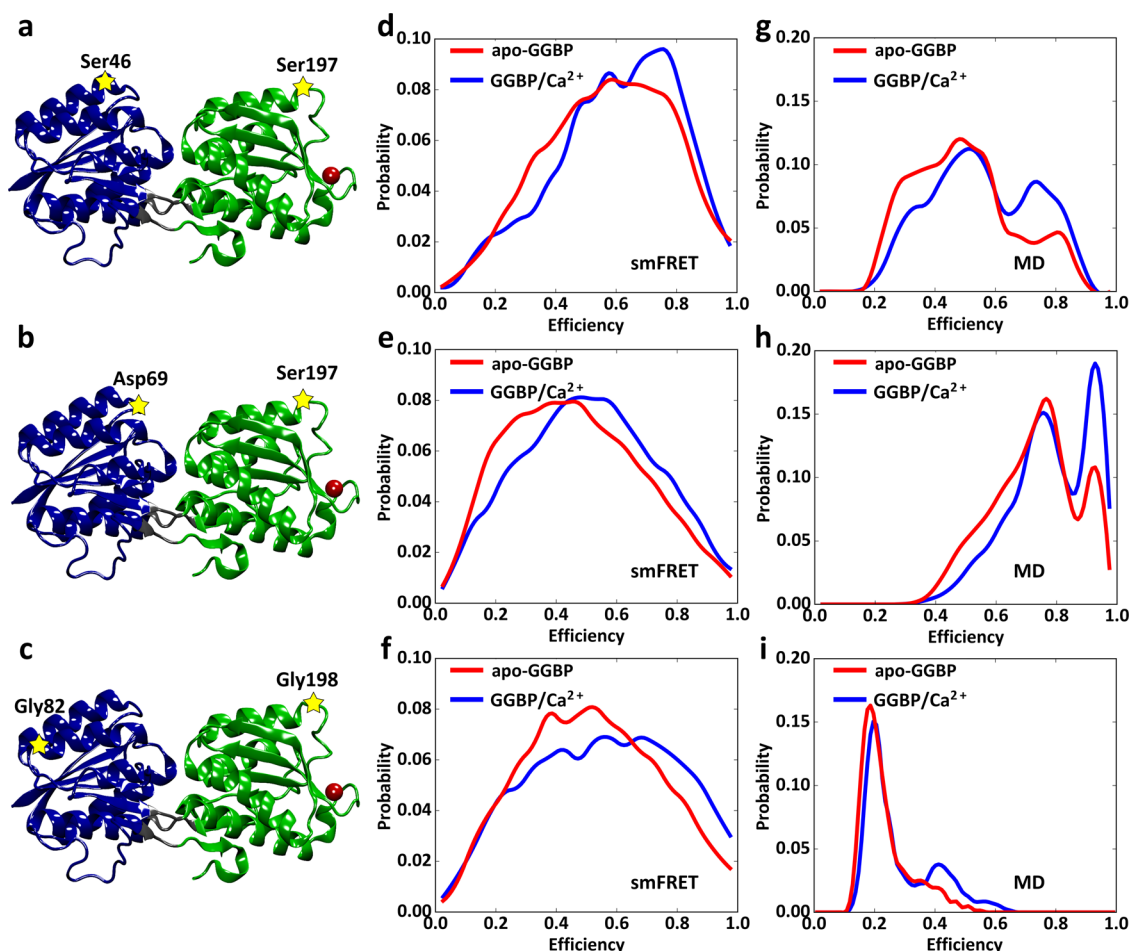


**Figure 2.** smFRET experiments of apo-GGBP and GGBP/Ca<sup>2+</sup>. (a–c) Diagrams showing the positions of labeled fluorescence dyes on GGBP (yellow stars). (d–f) smFRET efficiency distributions for the three labeling systems of apo-GGBP and GGBP/Ca<sup>2+</sup>, respectively. (g–i) MD simulation-derived smFRET efficiency distributions converted from  $C_{\alpha}$  distances between the labeled residues.

and bending angle:  $135^{\circ}\sim 150^{\circ}$ , twisting angle:  $0^{\circ}\sim 60^{\circ}$ ) can be identified, corresponding to two distinct interdomain bending angles. We mapped the six crystal structures of GGBP (two open structures, 2FW0 and 2QW1, and four closed structures, 2FVY, 2HPH, 1GLG, and 2GBP) onto the 2D-PMF, which shows that all the structures are consistent with the two energy minima. The energy barrier between the two energy minima is  $\sim 2$  kJ/mol, suggesting that apo-GGBP converts easily between the two conformations. In addition, the free energy landscape is very flat. The bending and twisting angles could vary in a range of  $180^{\circ}$  with less than 8 kJ/mol free energy costs (Figure 1b). Therefore, the information on the 2D-PMF suggests that apo-GGBP samples a large conformational space entailing significant interdomain motions (Figure 1b and Figure S5). This is consistent with the previous MD simulation studies of GGBP, where substantial opening-closing motions were observed in trajectories of only hundreds of nanoseconds.<sup>22</sup>

**Ca<sup>2+</sup> Binding Shifts the Conformational Equilibrium to the Open State.** For the GGBP/Ca<sup>2+</sup> system, we also performed three rounds of all-atom MD simulations with a total simulation time of 48.82  $\mu$ s, and constructed a 200-state MSM (Figures S1b and S2b, see Methods for more details). The 2D-PMFs show that apo-GGBP and GGBP/Ca<sup>2+</sup> sample a similar conformational space, but the equilibrium populations of the conformations are dramatically changed upon Ca<sup>2+</sup> binding (Figure 1b,c). The closed conformation becomes

unstable and the corresponding energy minimum disappeared (Figure 1c), suggesting that Ca<sup>2+</sup> binding significantly stabilizes the open conformation of GGBP.

To verify the simulation results, we performed smFRET measurements for apo-GGBP and GGBP/Ca<sup>2+</sup>. We generated three pairs of labeling sites for the FRET donor and acceptor (Ser46/Ser197, Asp69/Ser197, and Gly82/Gly198) by mutating them to cysteine (Figure 2a–c). Upon Ca<sup>2+</sup> binding, the efficiency distribution histograms of the three systems (Ser46/Ser197, Asp69/Ser197, and Gly82/Gly198) show obvious shifts toward lower values (Figure 2d–f), indicating the preference of the open state conformation. To compare the smFRET measurements with MD simulations, the distance distributions of inter-residue  $C_{\alpha}$  atoms were calculated and converted to FRET efficiencies (see Methods for more details). Although the efficiency distributions of MD simulations are narrower, the shifts upon Ca<sup>2+</sup> binding were qualitatively consistent with experiments (Figure 2g–i). Notably, the agreement between experiments and simulations is only qualitative. The distance distributions of smFRET measurement have a systematic deviation from those of the MD simulations. Such discrepancy could be caused by the errors from both experiment and simulation. From the simulation side, The MD simulation systems did not explicitly include the fluorophores since the large size of the dye molecules would significantly increase the computational costs. From the

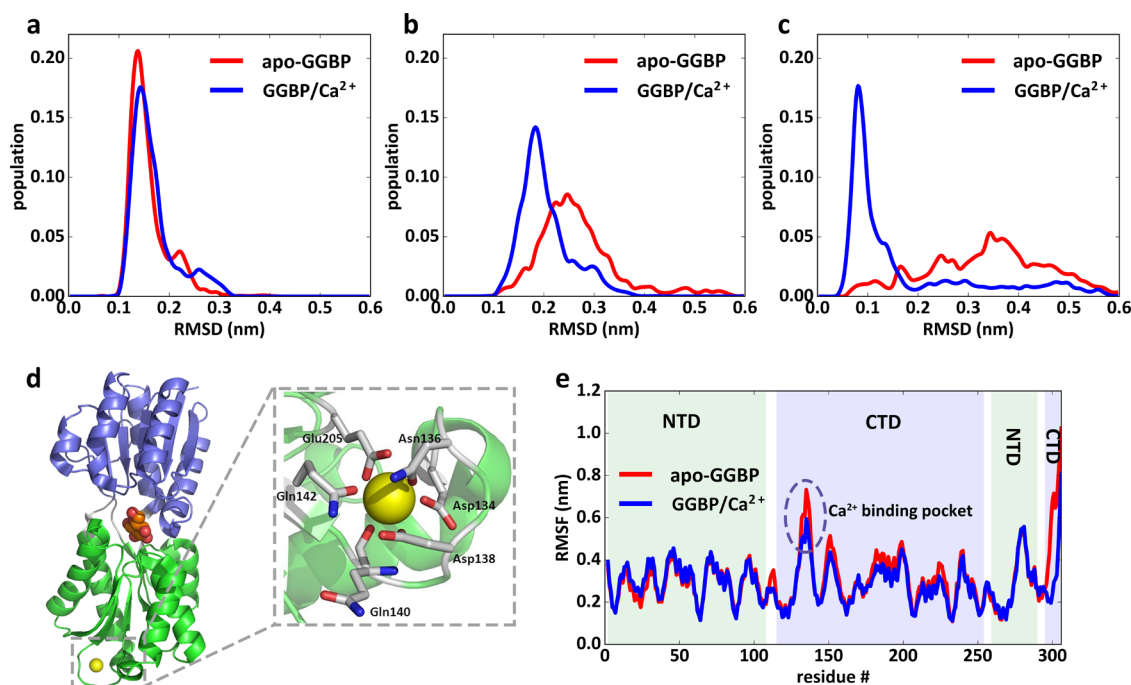


**Figure 3.** Ca<sup>2+</sup> binding mainly affects the structure of the C-terminal domain of GGBP. C $\alpha$ -RMSDs of the N-terminal domain (a), C-terminal domain (b), and Ca<sup>2+</sup>-binding pocket (c) of apo-GGBP (red) and GGBP/Ca<sup>2+</sup> (blue) with respect to the crystal structure with an open conformation (PDB ID: 2fw0). (d) Crystal structure (PDB ID: 2fw0) of GGBP/Ca<sup>2+</sup>, with the close-up view of the Ca<sup>2+</sup>-binding site. (e) C $\alpha$ -RMSFs of apo-GGBP (red) and GGBP/Ca<sup>2+</sup> (blue) systems.

experimental side, errors include the uncertainty in FRET efficiency measurements, and the variations of effective Förster radius  $R_0$  because of anisotropic tumbling of the donor and acceptor fluorophores, or changes in the donor quantum yield.  $R_0$  is proportional to the sixth roots of the orientation factor  $\kappa^2$  and the donor quantum yield  $Q_D$ . The orientation factor  $\kappa^2$ , which is assigned a value of 0.67 based on an assumption that perfect isotropic tumbling can in fact sample a wide range of values.

**Influence of Ca<sup>2+</sup>-Binding on the Local Structure around the Ca<sup>2+</sup>-Binding Site.** Previous studies showed that Ca<sup>2+</sup> helps stabilize the structure of GGBP.<sup>27,28</sup> We also characterized the structural stabilities of apo-GGBP and GGBP/Ca<sup>2+</sup> with NMR spectroscopy. By titrating Ca<sup>2+</sup> into apo-GGBP and recording <sup>1</sup>H-<sup>15</sup>N HSQC spectra, we found that Ca<sup>2+</sup> induced few chemical shift changes, while some peaks became sharper or appeared upon Ca<sup>2+</sup> binding (Figure S6). This indicates that Ca<sup>2+</sup> coordination indeed stabilized the structure of GGBP. To explore the influence of Ca<sup>2+</sup> binding in detail, the C $\alpha$ -RMSDs of each domain and the Ca<sup>2+</sup>-binding pocket with respect to the crystal structure were calculated using the MD simulation data. For both apo-GGBP and GGBP/Ca<sup>2+</sup> systems, the C $\alpha$ -RMSD distribution profiles of N-terminal domain are narrow (Figure 3a), indicating that the N-terminal domain is rigid and Ca<sup>2+</sup> binding barely influences the structure. On the other hand, the C $\alpha$ -RMSD distributions of the C-terminal domain are obviously different for the two systems (Figure 3b), showing that removing Ca<sup>2+</sup> leads to the C-terminal domain structure deviating from the crystal structure. The deviations are mainly located at the Ca<sup>2+</sup>-binding pocket, the C $\alpha$ -RMSDs of which exhibits large differences between the two systems (Figure 3c), and the C $\alpha$ -RMSD distribution of apo-GGBP is much broader than that of GGBP/Ca<sup>2+</sup>. We also calculated the C $\alpha$  root-mean-

square fluctuation (RMSF) from the MSM snapshots, which shows that generally the C-terminal domain of apo-GGBP has higher structural flexibility than that of GGBP/Ca<sup>2+</sup>, especially at the Ca<sup>2+</sup>-binding pocket (Figure 3e). Apparently, the motion of the Ca<sup>2+</sup>-binding loop is limited by the coordination of Ca<sup>2+</sup> (Figure 3d,e). We further characterized the changes of the binding pocket by calculating the solvent-accessible surface area (SASA) and inter-residue distances of the binding pocket. It turns out that Ca<sup>2+</sup>-binding reduces the SASA of the binding pocket and restricts the motions of the residues inside the pocket (Figures S7 and S8). This result is consistent with the previous experimental studies.<sup>27,28</sup> Therefore, Ca<sup>2+</sup> binding has an obvious effect on stabilizing the local structure of the Ca<sup>2+</sup>-binding site and the C-terminal domain, as well as on confining the protein conformation at the open state. The next question is how Ca<sup>2+</sup> regulates the interdomain movement through stabilizing the local structure of the C-terminal domain.

**Mechanism of the Regulation Role of Ca<sup>2+</sup>-Binding.** To explore the underlying regulation mechanism of Ca<sup>2+</sup> binding, we employed the community network method that characterizes the potential allosteric pathway by clustering residues into communities based on their correlation and proximity.<sup>60,61,63,68</sup> We built the community networks for apo-GGBP and GGBP/Ca<sup>2+</sup> systems based on their MSM ensembles (Figure 4). Figure 4a,b shows the coarse-grained picture of the community maps. The thickness of the edges between communities denotes the intercommunity “betweenness,” i.e., the strength of their dynamic coupling (see Methods). The two networks show slightly different community organizations. The network of apo-GGBP gives rise to one more community than that of GGBP/Ca<sup>2+</sup> (nine vs eight). The community boundaries in the C-terminal domain exhibit minor changes upon Ca<sup>2+</sup> binding by reassigning a few residues of c6, c7, c8, and c9 into the newly formed

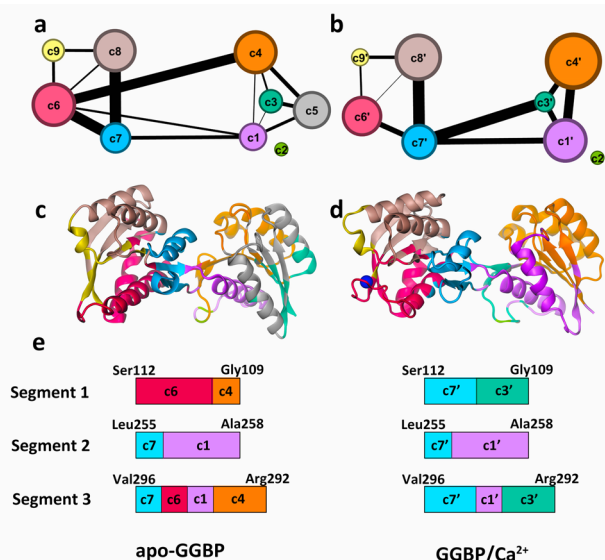


**Figure 4.** Optimal community networks of apo-GGBP and GGBP/Ca<sup>2+</sup>. Coarse-grained pictures of the dynamic network of apo-GGBP (a) and GGBP/Ca<sup>2+</sup> (b). The width of the bounds between communities is proportional to the total betweenness of intercommunities. The color-coded communities of apo-GGBP (b) and GGBP/Ca<sup>2+</sup> (d) are mapped onto the GGBP structure. (e) is the community assignment of three segments of the hinge regions.

communities c6', c7', c8', and c9'. The thickness of edges between c6'-c7' and c6'-c8' decreased with respect to those in apo-GGBP. Ca<sup>2+</sup> binding induced more obvious changes in the community organization of the N-terminal domain. The number of communities decreased from five to four. Communities c3 and c5 disappeared and merged with c1 and c4, giving rise to the new c1' and c4' communities with larger sizes (Figure 4c,d, Figure S9). The newly formed c3' is not a counterpart of c3. It is mainly composed of a small part from c4, including the long loop connecting the last  $\alpha$ -helix and the last  $\beta$ -strand of N-terminal domain and a short strand that precedes the first segment of the hinge region. Therefore, Ca<sup>2+</sup> binding leads to fewer communities and thicker edges connecting them, suggesting that the intradomain couplings within the N-terminal domain are stronger.

The most prominent change of the network upon Ca<sup>2+</sup> binding, however, is the interdomain communications in the hinge region. The community organization in the hinge region experiences delicate changes upon Ca<sup>2+</sup> binding. As shown in Figure 4e, the first segment of the hinge (Gly109-Ser112) in apo-GGBP is partitioned into c4 and c6, which are connected by an edge of the strongest interdomain coupling in apo-GGBP (Figure 4a). Upon Ca<sup>2+</sup> binding, the community composition of this segment changes to c3' and c7' (Figure 4e), the edge between which also exhibits the strongest interdomain coupling (Figure 4b). As mentioned above, c3' is composed of a very small part of c4, while c4' encompasses the largest component of the N-terminal domain. Therefore, the community reorganization of segment 1 (Gly109-Ser112) eliminates the direct coupling between the two large communities (c4 and c6) of N- and C-terminal domains. In another word, the large-scale interdomain cooperativity is weakened by Ca<sup>2+</sup> coordination. The community composition of segment 2 (Leu255-Ala258) barely changed upon Ca<sup>2+</sup> binding (Figure 4e). As for segment 3 (Arg292-Val296), the

community composition changed from c4-c1-c6-c7 to c3'-c1'-c7' upon Ca<sup>2+</sup> binding (Figure 4e). Similar to the case of segment 1, c4 is replaced by c3' and c6 disappears in segment 3. It is worth noting that the Ca<sup>2+</sup>-binding site is located in c6, which loses direct coupling with the N-terminal domain upon Ca<sup>2+</sup> binding. Overall, the hinge region plays a key role in the communications between N- and C-terminal domains. All three segments are at the interfaces of the N- and C-terminal domain communities. Ca<sup>2+</sup> binding changes the long-range interdomain correlations into more local correlations around the hinge region. If we assume that the interdomain opening-closing motion implicates cooperative movement of the two domains, the weakened interdomain coupling may explain the preference of the open conformation in GGBP/Ca<sup>2+</sup>.

As a complementary analysis, we further calculated the generalized correlation coefficients to explore more details (Figure 5). In line with the above analysis, the long-range

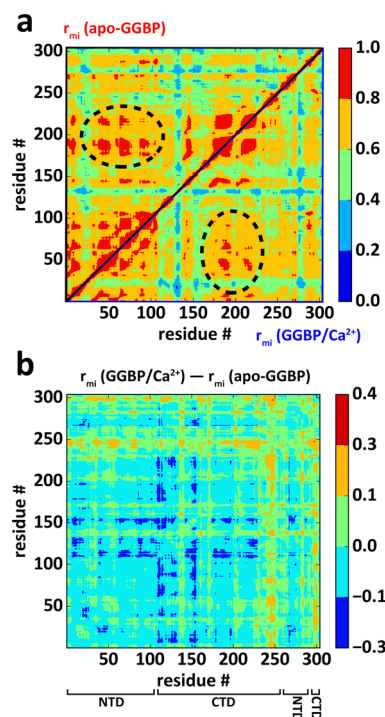


**Figure 5.** Inter-residue correlation analysis. The generalized correlation coefficients  $r_{MI}$  for apo-GGBP (upper diagonal of (a)), and GGBP/Ca<sup>2+</sup> (lower diagonal of (a)). (b) Difference of  $r_{MI}$  between GGBP/Ca<sup>2+</sup> and apo-GGBP. The positive/negative values denote the enhanced/reduced inter-residue correlations upon Ca<sup>2+</sup> binding, respectively. Regions with prominent changes mentioned in the main text are highlighted by red dashed ovals.

interdomain correlations are obviously impaired by Ca<sup>2+</sup> binding (Figure 5a, highlighted with dashed ovals). Additionally, the correlations of the regions flanking the Ca<sup>2+</sup>-binding loop, i.e., the  $\alpha$ -helix (Lys113-Asn130) and the  $\beta$ -strand (Ile141-Lys147) (part of community c6/c6'), with the N-terminal domain and part of the C-terminal domain were obviously weakened upon Ca<sup>2+</sup> binding (Figure 5b, dark blue). On the other hand, Ca<sup>2+</sup> binding increases the correlations between residues in c7/c7' and most of the other parts of the protein (Figure 5b, orange color).

Both community network and generalized correlation coefficients calculations indicate the weakened correlations of



the  $\text{Ca}^{2+}$ -binding site and its flanking region (belong to c6/c6' community) with the N-terminal domain and other part of the C-terminal domain. This could directly result from  $\text{Ca}^{2+}$  coordination. We compared the hydrogen bonding interactions of apo-GGBP and GGBP/ $\text{Ca}^{2+}$  systems (Table S2). The main differences are within the C-terminal domain. The frequencies of 51 hydrogen bonds decreased or increased at least 10% after  $\text{Ca}^{2+}$  binding. As expected, the hydrogen bonds near the  $\text{Ca}^{2+}$ -binding pocket are enhanced upon  $\text{Ca}^{2+}$  binding (Table S2). While the hydrogen bonding network around the  $\text{Ca}^{2+}$ -binding site is strengthened, some hydrogen bonding interactions related to the C-terminal domain are weakened (Figure 5 and Table S2). For example, the hydrogen bonds (Ser115-OG:Asp111-O, Ser115-N:Asp111-O) between the C-terminal domain and the hinge region are significantly reduced by ~20% after  $\text{Ca}^{2+}$  binding. This may partly account for the loss of connections of the c6' community with other parts of the protein. Notably, the residue Ser115 is near the N-termini of  $\alpha$ -helix (Lys113-Asn130), which directly connects the hinge region and the  $\text{Ca}^{2+}$ -binding loop (Figure S10). Another hydrogen bond (Ala237-N:Val254-O), which is within c7' community, also decreased by 20% upon  $\text{Ca}^{2+}$  binding (Table S2).

Overall, the coordination of  $\text{Ca}^{2+}$  stabilizes the structure around the binding site and strengthens the local hydrogen bonds. At the same time, the long-range interdomain correlations are weakened, which may explain the preference of the open conformation. To examine the effect of  $\text{Ca}^{2+}$  on sugar-binding affinity, we performed isothermal titration calorimetry (ITC) measurements. In the presence of  $\text{Ca}^{2+}$ , the binding affinity of glucose to GGBP ( $K_D = 490 \pm 159$  nM) is almost the same as that of the apo-GGBP ( $K_D = 492 \pm 84$  nM) (Figure S11). Therefore, it seems that  $\text{Ca}^{2+}$  binding does not affect the ligand binding of GGBP.

## DISCUSSION

Previous studies have shown the role of calcium in stabilizing the structure of GGBP.<sup>27,28</sup> This effect is especially prominent when GGBP is free of sugar substrates. Our simulation results agree with the experimental observations that the depletion of  $\text{Ca}^{2+}$  results in structural fluctuations in the  $\text{Ca}^{2+}$ -binding site and the C-terminal domain of GGBP. More interesting insights are obtained from the MSM analysis. The coordination of  $\text{Ca}^{2+}$  was found to shift the conformational population of GGBP toward the open state. This suggests that the role of  $\text{Ca}^{2+}$  is not only in the maintenance of the structure integrity but also in the regulation of large-scale conformational dynamics. MSM analysis allows us to quantitatively probe the distribution of conformational states and their interconversion kinetics. Although the closed state is still accessible in the GGBP/ $\text{Ca}^{2+}$  system, the population of the closed state is significantly reduced upon  $\text{Ca}^{2+}$  binding. We further lumped the 200-state MSM into two macrostates, an open state and a closed state (Figure S12), and the population shift upon  $\text{Ca}^{2+}$  binding is about 12.05% (Figure S13). This population shift originates from the slower open-to-closed transition (mean first passage time (MFPT) =  $569.1 \pm 15.6$  ns) in the GGBP/ $\text{Ca}^{2+}$  system than the case of apo-GGBP (MFPT =  $387.9 \pm 10.7$  ns). In the previous MD simulation study,<sup>22</sup> the time scale of the conversion between the open and closed conformations was estimated to be around 25 ns, which is much shorter than our MSM estimation. Since the MD sampling in this work is much more sufficient and the MSM analysis is a more rigorous

method for retrieving kinetic information, we anticipate that the exchange rate obtained here is more accurate.

The community network analysis provided hints of the mechanism of  $\text{Ca}^{2+}$ -binding-regulated protein dynamics. The coordination of  $\text{Ca}^{2+}$  strengthens the local structural stability and dynamic couplings and attenuates the long-range cooperativity in the interdomain conformational motions. It is intriguing that  $\text{Ca}^{2+}$  binding induces delicate changes of the dynamic behavior of the hinge region, suggesting an allosteric regulatory mechanism. In another word, the property of the hinge and thereby the conformational dynamics of protein could be modulated by a remote site instead of the direct mutations at the hinge region. This may provide hints in the biosensor design of GGBP. It should be noted that the above analysis could not exclude the alternative scenario that the two domains move more freely independent of each other upon the weakened interdomain couplings. To establish a concrete explanation of how weakened coupling changes the free energy landscape requires more rigorous analysis of the residue-specific contribution of the free energy changes, which might be a subject of future work.

The stabilization of the open conformation of GGBP upon  $\text{Ca}^{2+}$  binding is shown to have no effect on the substrate-binding affinity. This observation indicates that the functional role of  $\text{Ca}^{2+}$  is not related to substrate binding. Since the concentration of  $\text{Ca}^{2+}$  ions in the periplasm is close to the extracellular value (at the mM level), GGBP should be  $\text{Ca}^{2+}$ -saturated most of the time. However, as an invasive glucose biosensor, GGBP is often used in the presence of a strong chelating agent of calcium, such as EDTA.<sup>27</sup> Our study suggests that even in a low concentration of  $\text{Ca}^{2+}$ , GGBP could still maintain its capacity as a sugar biosensor. Another possible functional role of  $\text{Ca}^{2+}$  binding could be associated with the active transport of glucose/galactose. It was proposed that only the closed conformation of GGBP could recognize the related membrane transporter. Stabilization of the open conformation of the unliganded GGBP could reduce the nonproductive association with the membrane transporter.

## CONCLUSIONS

In this study, we performed extensive MD simulations and MSM analysis to decipher the role of  $\text{Ca}^{2+}$  in the stability and dynamics of GGBP. It has been found that  $\text{Ca}^{2+}$  binding stabilizes the local structure of the C-terminal domain and simultaneously regulates the large-scale conformational dynamics of GGBP by shifting the conformational state equilibrium toward the open conformation. The community network analysis discloses how  $\text{Ca}^{2+}$  binding regulates the interdomain motions by changing the local hydrogen bonding network and the dynamic coupling between the two domains. The conformational regulatory role of  $\text{Ca}^{2+}$  does not affect the ligand-binding affinity, suggesting that GGBP as a biosensor is able to work under low  $\text{Ca}^{2+}$  concentration conditions.

## ASSOCIATED CONTENT

### Supporting Information

The Supporting Information is available free of charge at <https://pubs.acs.org/doi/10.1021/acs.jcim.0c01119>.

Details of experimental and computational methods; variations of implied timescales; Chapman–Kolmogorov tests; box plot for GMRQ tests of the parameters for MSM construction; implied timescale and the calculated

free energy landscape of the 50-state MSM; time variations of the bending and twisting angles along a selected trajectory;  $^1\text{H}$ - $^{15}\text{N}$  HSQC spectra of apo-GGBP and GGBP/ $\text{Ca}^{2+}$ ; SASA distributions of the  $\text{Ca}^{2+}$ -binding pocket in apo-GGBP and GGBP/ $\text{Ca}^{2+}$ ; distance distributions of three atom pairs inside the  $\text{Ca}^{2+}$ -binding pocket; assignments of communities for all the residues in apo-GGBP and GGBP/ $\text{Ca}^{2+}$  systems; hydrogen bonds between Ser115 and Asp111; ITC experiments that measure the glucose binding affinities; two-state MSM for apo-GGBP and GGBP/ $\text{Ca}^{2+}$ ; populations of the closed and open states in the two-state MSM; details of the simulation systems; variations of hydrogen bonds upon  $\text{Ca}^{2+}$  binding (PDF)

## AUTHOR INFORMATION

### Corresponding Authors

**Jingwei Weng** – Department of Chemistry, Multiscale Research Institute of Complex Systems and Institute of Biomedical Sciences, Fudan University, Shanghai 200438, China; Email: [jwweng@fudan.edu.cn](mailto:jwweng@fudan.edu.cn)

**Zhijun Liu** – National Facility for Protein Science in Shanghai, Zhangjiang Lab, Shanghai Advanced Research Institute, Chinese Academy of Sciences, Shanghai 201210, China; Email: [liuzhijun@sari.ac.cn](mailto:liuzhijun@sari.ac.cn)

**Wenning Wang** – Department of Chemistry, Multiscale Research Institute of Complex Systems and Institute of Biomedical Sciences, Fudan University, Shanghai 200438, China; [orcid.org/0000-0002-8712-0536](https://orcid.org/0000-0002-8712-0536); Email: [wnwang@fudan.edu.cn](mailto:wnwang@fudan.edu.cn)

### Authors

**Maohua Yang** – Department of Chemistry, Multiscale Research Institute of Complex Systems and Institute of Biomedical Sciences, Fudan University, Shanghai 200438, China

**Yegen Tang** – Department of Chemistry, Multiscale Research Institute of Complex Systems and Institute of Biomedical Sciences, Fudan University, Shanghai 200438, China

Complete contact information is available at:  
<https://pubs.acs.org/10.1021/acs.jcim.0c01119>

### Author Contributions

#M.Y. and Y.T. contributed equally to the work. W.W. and Z.L. conceived and designed the project. M.Y. performed computational studies. Y.T. and Z.L. performed the biochemical, smFRET, ITC, and NMR experiments. M.Y., Y.T., J.W., and Z.L. analyzed the simulation and experimental results. M.Y., J.W., Z.L., and W.W. prepared the manuscript. All authors contributed to data interpretation.

### Notes

The authors declare no competing financial interest.

## ACKNOWLEDGMENTS

The authors thank the Ministry of Science and Technology of the People's Republic of China (2016YFA0501702), National Natural Science Foundation of China (21773038 and 22073018), Shanghai Municipal Science and Technology Major Project (No. 2018SHZDZX01) and Zhangjiang Lab Foundation (Grant no. Y93Z011D01 to Z. L.) for financial support. The authors also thank the staff at the National

Facility for Protein Science in Shanghai, for providing technical support in NMR data collection and analysis.

## ABBREVIATIONS

ABC, ATP-binding cassette; CTD, C-terminal domain; EDTA, ethylenediaminetetraacetic acid; GGBP, D-glucose/D-galactose-binding protein; ITC, isothermal titration calorimetry; MD simulation, molecular dynamics simulation; MSM, Markov state model; NMR, nuclear magnetic resonance; NTD, N-terminal domain; PDB, protein data bank; PMF, potential of mean force; RMSD, root-mean-square deviation; RMSE, root-mean-square fluctuation; SASA, solvent-accessible surface area; SBP, substrate-binding protein; smFRET, single-molecule Förster resonance energy transfer

## REFERENCES

- (1) Berger, E. A. Different mechanisms of energy coupling for the active transport of proline and glutamine in *Escherichia coli*. *Proc. Natl. Acad. Sci.* **1973**, *70*, 1514–1518.
- (2) Berger, E. A.; Heppel, L. A. Different mechanisms of energy coupling for the shock-sensitive and shock-resistant amino acid permeases of *Escherichia coli*. *J. Biol. Chem.* **1974**, *249*, 7747–7755.
- (3) Tam, R.; Saier, M. H. J. Structural, functional, and evolutionary relationships among extracellular solute-binding receptors of bacteria. *Microbiol. Rev.* **1993**, *57*, 320–346.
- (4) Felder, C. B.; Graul, R. C.; Lee, A. Y.; Merkle, H. P.; Sadee, W. The venus flytrap of periplasmic binding proteins: An ancient protein module present in multiple drug receptors. *AAPS PharmSci* **1999**, *1*, No. E2.
- (5) Higgins, C. F.; Linton, K. J. ABC transporters: An introduction and overview. In *ABC proteins*, Holland, I. B.; Cole, S. P. C.; Kuchler, K.; Higgins, C. F., Eds.; Academic Press: London, 2003; xvii–xxiii.
- (6) Neiditch, M. B.; Federle, M. J.; Pompeani, A. J.; Kelly, R. C.; Swem, D. L.; Jeffrey, P. D.; Bassler, B. L.; Hughson, F. M. Ligand-induced asymmetry in histidine sensor kinase complex regulates quorum sensing. *Cell* **2006**, *126*, 1095–1108.
- (7) Gonin, S.; Arnoux, P.; Pierru, B.; Laverne, J.; Alonso, B.; Sabaty, M.; Pignol, D. Crystal structures of an extracytoplasmic solute receptor from a trap transporter in its open and closed forms reveal a helix-swapped dimer requiring a cation for alpha-keto acid binding. *BMC Struct. Biol.* **2007**, *7*, 11.
- (8) Mulligan, C.; Geertsma, E. R.; Severi, E.; Kelly, D. J.; Poolman, B.; Thomas, G. H. The substrate-binding protein imposes directionality on an electrochemical sodium gradient-driven trap transporter. *Proc. Natl. Acad. Sci.* **2009**, *106*, 1778–1783.
- (9) Berntsson, R. P.-A.; Smits, S. H. J.; Schmitt, L.; Slotboom, D. J.; Poolman, B. A structural classification of substrate-binding proteins. *FEBS Lett.* **2010**, *584*, 2606–2617.
- (10) Quirocho, F. A.; Ledvina, P. S. Atomic structure and specificity of bacterial periplasmic receptors for active transport and chemotaxis: Variation of common themes. *Mol. Microbiol.* **1996**, *20*, 17–25.
- (11) Fukami-Kobayashi, K.; Tateno, Y.; Nishikawa, K. Domain dislocation: A change of core structure in periplasmic binding proteins in their evolutionary history. *J. Mol. Biol.* **1999**, *286*, 279–290.
- (12) Scheepers, G. H.; Lycklama, A. N. J. A.; Poolman, B. An updated structural classification of substrate-binding proteins. *FEBS Lett.* **2016**, *590*, 4393–4401.
- (13) Anraku, Y. Transport of sugars and amino acids in bacteria. I. Purification and specificity of the galactose- and leucine-binding proteins. *J. Biol. Chem.* **1968**, *243*, 3116–3122.
- (14) Hazelbauer, G. L.; Adler, J. Role of the galactose binding protein in chemotaxis of *Escherichia coli* toward galactose. *Nat. New Biol.* **1971**, *230*, 101–104.
- (15) Vyas, N. K.; Vyas, M. N.; Quirocho, F. A. The 3 Å resolution structure of a D-galactose-binding protein for transport and chemotaxis in *Escherichia coli*. *Proc. Natl. Acad. Sci.* **1983**, *80*, 1792–1796.



- (16) Vyas, N. K.; Vyas, M. N.; Quirocho, F. A. A novel calcium binding site in the galactose-binding protein of bacterial transport and chemotaxis. *Nature* **1987**, *327*, 635–638.
- (17) Vyas, N.; Vyas, M.; Quirocho, F. Sugar and signal-transducer binding sites of the escherichia coli galactose chemoreceptor protein. *Science (New York, N.Y.)* **1988**, *242*, 1290–1295.
- (18) Vyas, M. N.; Vyas, N. K.; Quirocho, F. A. Crystallographic analysis of the epimeric and anomeric specificity of the periplasmic transport/chemosensory protein receptor for d-glucose and d-galactose. *Biochemistry* **1994**, *33*, 4762–4768.
- (19) Borrok, M. J.; Kiessling, L. L.; Forest, K. T. Conformational changes of glucose/galactose-binding protein illuminated by open, unliganded, and ultra-high-resolution ligand-bound structures. *Protein Sci.* **2007**, *16*, 1032–1041.
- (20) Borrok, M. J.; Zhu, Y.; Forest, K. T.; Kiessling, L. L. Structure-based design of a periplasmic binding protein antagonist that prevents domain closure. *ACS Chem. Biol.* **2009**, *4*, 447–456.
- (21) Ortega, G.; Castaño, D.; Diercks, T.; Millet, O. Carbohydrate affinity for the glucose-galactose binding protein is regulated by allosteric domain motions. *J. Am. Chem. Soc.* **2012**, *134*, 19869–19876.
- (22) Unione, L.; Ortega, G.; Mallagaray, A.; Corzana, F.; Pérez-Castells, J.; Canales, A.; Jiménez-Barbero, J.; Millet, O. Unraveling the conformational landscape of ligand binding to glucose/galactose-binding protein by paramagnetic NMR and MD simulations. *ACS Chem. Biol.* **2016**, *11*, 2149–2157.
- (23) Marvin, J. S.; Hellinga, H. W. Engineering biosensors by introducing fluorescent allosteric signal transducers: Construction of a novel glucose sensor. *J. Am. Chem. Soc.* **1998**, *120*, 7–11.
- (24) Sacks, D. B.; Bruns, D. E.; Goldstein, D. E.; Maclaren, N. K.; McDonald, J. M.; Parrott, M. Guidelines and recommendations for laboratory analysis in the diagnosis and management of diabetes mellitus. *Clin. Chem.* **2002**, *48*, 436–472.
- (25) Amiss, T. J.; Sherman, D. B.; Nycz, C. M.; Andaluz, S. A.; Pitner, J. B. Engineering and rapid selection of a low-affinity glucose/galactose-binding protein for a glucose biosensor. *Protein Sci.* **2007**, *16*, 2350–2359.
- (26) Domínguez, D. C.; Guragain, M.; Patrauchan, M. Calcium binding proteins and calcium signaling in prokaryotes. *Cell Calcium* **2015**, *57*, 151–165.
- (27) Herman, P.; Vecer, J.; Barvik, I., Jr.; Scognamiglio, V.; Staiano, M.; de Champdore, M.; Varriale, A.; Rossi, M.; D'Auria, S. The role of calcium in the conformational dynamics and thermal stability of the d-galactose/d-glucose-binding protein from Escherichia coli. *Proteins Struct. Funct. Bioinform.* **2005**, *61*, 184–195.
- (28) D'Auria, S.; Ausili, A.; Marabotti, A.; Varriale, A.; Scognamiglio, V.; Staiano, M.; Bertoli, E.; Rossi, M.; Tanfani, F. Binding of glucose to the d-galactose/d-glucose-binding protein from Escherichia coli restores the native protein secondary structure and thermostability that are lost upon calcium depletion. *J. Biochem.* **2006**, *139*, 213–221.
- (29) Stepanenko, O. V.; Stepanenko, O. V.; Povarova, O. I.; Fonin, A. V.; Kuznetsova, I. M.; Turoverov, K. K.; Staiano, M.; Varriale, A.; D'Auria, S. New insight into protein-ligand interactions. The case of the d-galactose/d-glucose-binding protein from Escherichia coli. *J. Phys. Chem. B* **2011**, *115*, 2765–2773.
- (30) Zwier, M. C.; Chong, L. T. Reaching biological timescales with all-atom molecular dynamics simulations. *Curr. Opin. Pharmacol.* **2010**, *10*, 745–752.
- (31) Bowman, G. R.; Huang, X.; Pande, V. S. Using generalized ensemble simulations and Markov state models to identify conformational states. *Methods* **2009**, *49*, 197–201.
- (32) Noé, F.; Schütte, C.; Vanden-Eijnden, E.; Reich, L.; Weikl, T. R. Constructing the equilibrium ensemble of folding pathways from short off-equilibrium simulations. *Proc. Natl. Acad. Sci.* **2009**, *106*, 19011–19016.
- (33) Pande, V. S.; Beauchamp, K.; Bowman, G. R. Everything you wanted to know about Markov state models but were afraid to ask. *Methods* **2010**, *52*, 99–105.
- (34) Shukla, D.; Hernández, C. X.; Weber, J. K.; Pande, V. S. Markov state models provide insights into dynamic modulation of protein function. *Acc. Chem. Res.* **2015**, *48*, 414–422.
- (35) Husic, B. E.; Pande, V. S. Markov state models: From an art to a science. *J. Am. Chem. Soc.* **2018**, *140*, 2386–2396.
- (36) Schneider, J. P.; Pochan, D. J.; Ozbas, B.; Rajagopal, K.; Pakstis, L.; Kretsinger, J. Responsive hydrogels from the intramolecular folding and self-assembly of a designed peptide. *J. Am. Chem. Soc.* **2002**, *124*, 15030–15037.
- (37) Jayachandran, G.; Vishal, V.; Pande, V. S. Using massively parallel simulation and markovian models to study protein folding: Examining the dynamics of the villin headpiece. *J. Chem. Phys.* **2006**, *124*, No. 164902.
- (38) Husic, B. E.; McGibbon, R. T.; Sultan, M. M.; Pande, V. S. Optimized parameter selection reveals trends in Markov state models for protein folding. *J. Chem. Phys.* **2016**, *145*, No. 194103.
- (39) Silva, D. A.; Bowman, G. R.; Sosa-Peinado, A.; Huang, X. A role for both conformational selection and induced fit in ligand binding by the lao protein. *PLoS Comput. Biol.* **2011**, *7*, No. e1002054.
- (40) Bucher, D.; Grant, B. J.; McCammon, J. A. Induced fit or conformational selection? The role of the semi-closed state in the maltose binding protein. *Biochemistry* **2011**, *50*, 10530–10539.
- (41) Gu, S.; Silva, D. A.; Meng, L.; Yue, A.; Huang, X. Quantitatively characterizing the ligand binding mechanisms of choline binding protein using Markov state model analysis. *PLoS Comput. Biol.* **2014**, *10*, No. e1003767.
- (42) Feng, Y.; Zhang, L.; Wu, S.; Liu, Z.; Gao, X.; Zhang, X.; Liu, M.; Liu, J.; Huang, X.; Wang, W. Conformational dynamics of apoglnbp revealed by experimental and computational analysis. *Angew. Chem., Int. Ed.* **2016**, *55*, 13990–13994.
- (43) Weng, J.; Gu, S.; Gao, X.; Huang, X.; Wang, W. Maltose-binding protein effectively stabilizes the partially closed conformation of the ATP-binding cassette transporter malfgk 2. *Phys. Chem. Chem. Phys.* **2017**, *19*, 9366–9373.
- (44) Wang, D.; Weng, J.; Wang, W. An unconventional ligand-binding mechanism of substrate-binding proteins: MD simulation and Markov state model analysis of BTUF. *J. Comput. Chem.* **2019**, *40*, 1440–1448.
- (45) Noé, F.; Horenko, I.; Schütte, C.; Smith, J. C. Hierarchical analysis of conformational dynamics in biomolecules: Transition networks of metastable states. *J. Chem. Phys.* **2007**, *126*, No. 155102.
- (46) Zheng, W.; Andrec, M.; Gallicchio, E.; Levy, R. M. Recovering kinetics from a simplified protein folding model using replica exchange simulations: A kinetic network and effective stochastic dynamics. *J. Phys. Chem. B* **2009**, *113*, 11702–11709.
- (47) Qiao, Q.; Bowman, G. R.; Huang, X. Dynamics of an intrinsically disordered protein reveal metastable conformations that potentially seed aggregation. *J. Am. Chem. Soc.* **2013**, *135*, 16092–16101.
- (48) Weng, J.; Wang, W. Structural features and energetics of the periplasmic entrance opening of the outer membrane channel tolC revealed by molecular dynamics simulation and Markov state model analysis. *J. Chem. Inf. Model.* **2019**, *59*, 2359–2366.
- (49) Chodera, J. D.; Noé, F. Markov state models of biomolecular conformational dynamics. *Curr. Opin. Struct. Biol.* **2014**, *25*, 135–144.
- (50) Abraham, M. J.; Murtola, T.; Schulz, R.; Páll, S.; Smith, J. C.; Hess, B.; Lindahl, E. Gromacs: High performance molecular simulations through multi-level parallelism from laptops to supercomputers. *SoftwareX* **2015**, *1–2*, 19–25.
- (51) Sorin, E. J.; Pande, V. S. Exploring the helix-coil transition via all-atom equilibrium ensemble simulations. *Biophys. J.* **2005**, *88*, 2472–2493.
- (52) Jorgensen, W. L.; Chandrasekhar, J.; Madura, J. D.; Impey, R. W.; Klein, M. L. Comparison of simple potential functions for simulating liquid water. *J. Chem. Phys.* **1983**, *79*, 926–935.
- (53) Berendsen, H. J. C.; Postma, J. P. M.; van Gunsteren, W. F.; DiNola, A.; Haak, J. R. Molecular dynamics with coupling to an external bath. *J. Chem. Phys.* **1984**, *81*, 3684–3690.

- (54) Hess, B.; Bekker, H.; Berendsen, H. J.; Fraaije, J. G. Lincs: A linear constraint solver for molecular simulations. *J. Comput. Chem.* **1997**, *18*, 1463–1472.
- (55) Darden, T.; York, D.; Pedersen, L. Particle mesh ewald: An  $n \log(n)$  method for ewald sums in large systems. *J. Chem. Phys.* **1993**, *98*, 10089–10092.
- (56) Scherer, M. K.; Trendelkamp-Schroer, B.; Paul, F.; Pérez-Hernández, G.; Hoffmann, M.; Plattner, N.; Wehmeyer, C.; Prinz, J.-H.; Noé, F. Pyemma 2: A software package for estimation, validation, and analysis of Markov models. *J. Chem. Theory Comput.* **2015**, *11*, 5525–5542.
- (57) Harrigan, M. P.; Sultan, M. M.; Hernandez, C. X.; Husic, B. E.; Eastman, P.; Schwantes, C. R.; Beauchamp, K. A.; McGibbon, R. T.; Pande, V. S. Msmbuilder: Statistical models for biomolecular dynamics. *Biophys. J.* **2017**, *112*, 10–15.
- (58) Bowman, G. R.; Beauchamp, K. A.; Boxer, G.; Pande, V. S. Progress and challenges in the automated construction of Markov state models for full protein systems. *J. Chem. Phys.* **2009**, *131*, 124101.
- (59) Prinz, J. H.; Wu, H.; Sarich, M.; Keller, B.; Senne, M.; Held, M.; Chodera, J. D.; Schütte, C.; Noé, F. Markov models of molecular kinetics: Generation and validation. *J. Chem. Phys.* **2011**, *134*, 174105.
- (60) Rivalta, I.; Sultan, M. M.; Lee, N.-S.; Manley, G. A.; Loria, J. P.; Batista, V. S. Allosteric pathways in imidazole glycerol phosphate synthase. *Proc. Natl. Acad. Sci.* **2012**, *109*, E1428–E1436.
- (61) McClendon, C. L.; Kornev, A. P.; Gilson, M. K.; Taylor, S. S. Dynamic architecture of a protein kinase. *Proc. Natl. Acad. Sci.* **2014**, *111*, E4623–E4631.
- (62) Humphrey, W.; Dalke, A.; Schulten, K. VMD: Visual molecular dynamics. *J. Mol. Graph.* **1996**, *14*, 33–38.
- (63) Eargle, J.; Luthey-Schulten, Z. Networkview: 3d display and analysis of protein-RNA interaction networks. *Bioinformatics* **2012**, *28*, 3000–3001.
- (64) Girvan, M.; Newman, M. E. J. Community structure in social and biological networks. *Proc. Natl. Acad. Sci.* **2002**, *99*, 7821–7826.
- (65) Preus, S.; Noer, S. L.; Hildebrandt, L. L.; Gudnason, D.; Birkedal, V. Isms: Single-molecule fret microscopy software. *Nat. Methods* **2015**, *12*, 593–594.
- (66) Förster, T., *Experimental and theoretical investigation of the intermolecular transfer of electron excitation energy*. 1992.
- (67) Sasmal, D. K.; Pulido, L. E.; Kasal, S.; Huang, J. Single-molecule fluorescence resonance energy transfer in molecular biology. *Nano-scale* **2016**, *8*, 19928–19944.
- (68) Sethi, A.; Eargle, J.; Black, A. A.; Luthey-Schulten, Z. Dynamical networks in tRNA:Protein complexes. *Proc. Natl. Acad. Sci.* **2009**, *106*, 6620–6625.